

A comprehensive variable temperature study of the layered oxide, $\text{Ca}_2\text{Mn}_3\text{O}_8$

Laura J. Vera Stimpson,^a Jason A. McNulty,^b Finlay D. Morrison,^b Amit Mahajan,^c Emma E. McCabe,^a Alexandra S. Gibbs,^d Gavin B. G. Stenning,^d Marek Jura,^d and Donna C. Arnold,^{*a}

^a School of Physical Sciences, University of Kent, Canterbury, Kent, CT2 7NH, UK

^b School of Chemistry, University of St Andrews, North Haugh, St Andrews, Fife, KY16 9ST, Scotland, UK

^c School of Engineering and Materials Science, Queen Mary University of London, Mile End Road, London, E1 4NS, UK

^d ISIS Neutron and Muon Source, Rutherford Appleton Laboratory, Harwell Science and Innovation Campus, Didcot, OX11 0QX, UK

* Corresponding Author e-mail: d.c.arnold@kent.ac.uk, tel: 01227 827810

Abstract

$\text{Ca}_2\text{Mn}_3\text{O}_8$ forms a delafossite-related layered structure, which crystallises with monoclinic $C2/m$ symmetry. Compared with the delafossite-structure, the MnO_6 layers in $\text{Ca}_2\text{Mn}_3\text{O}_8$ exhibit an ordered cation void which forms a magnetic ‘bow-tie’ like connectivity of Mn^{4+} ion layers separated by Ca^{2+} ions. *In-situ* variable temperature diffraction data demonstrates that the structure is robust up to a temperature of approximately 1173 K before the material decomposes into the perovskite, CaMnO_3 and marokite, CaMn_2O_4 phases. Simultaneous thermal analysis suggests that a very small amount of water remains within the layers post synthesis. Impedance spectroscopy indicates that $\text{Ca}_2\text{Mn}_3\text{O}_8$ is an electronic conductor in the range $\sim 400 - 700$ K with an activation energy of 0.50 ± 0.01 eV.

1.0 Introduction

Layered transition metal oxides have attracted extensive attention within the literature primarily due to their wide-ranging potential for application arising as a result of their compositional flexibility [1]. For example, possible applications including in catalysis, optoelectronics, solar cells, functional windows, thermoelectrics and batteries have been reported for the ABX_2 layered materials (where A is typically a monovalent ion e.g. Cu^+ or Na^+ , B is a trivalent transition metal, e.g. Fe^{3+} , and X is normally O^{2-} e.g. CuFeO_2) [1-8]. Additionally, in materials containing magnetic species the potential for frustrated spin

connectivity (where the crystal topography does not allow for all antiferromagnetic pair ways interactions to be satisfied) has led to a wealth of interesting and exotic magnetic ground states in these materials [2,9]. The wide versatility and application of these materials therefore drives the search for continued understanding of structure-property relations and phase stability. Recently we have become interested in the layered material, $\text{Ca}_2\text{Mn}_3\text{O}_8$ [10,11]. $\text{Ca}_2\text{Mn}_3\text{O}_8$ is comprised of $\text{Mn}_3\text{O}_8^{4-}$ layers separated by Ca^{2+} ions (Figure 1). An ordered void in the manganese framework alternates between layers resulting in ABAB stacking in the lattice a direction as described in detail elsewhere [10-14]. The Ca-Mn-O phase diagram was studied in 1978 by Horowitz *et al* [15]. They prepared materials with various stoichiometries in both air and oxygen and determined the Ca-Mn-O ratios of the final products. Subsequently, they determined the decomposition routes by heating single phase materials (in either air or oxygen) to elevated temperatures before quenching the products and collecting diffraction data at room temperature [15]. These experiments predicted that $\text{Ca}_2\text{Mn}_3\text{O}_8$ could be expected to decompose into perovskite, CaMnO_3 and marokite, CaMn_2O_4 materials at ~ 1163 K in oxygen [15]. Later the same authors reported a detailed analysis of the structure and magnetic properties of this material, however, difficulties in preparing high quality bulk materials limited their investigation of the magnetic order [12-14]. More recently, as with other layered oxides, these materials have attracted attention as battery cathodes and as catalysts for water oxidation [16-23]. We have demonstrated that synthetic route can have a large effect on the morphology and crystallinity of the material obtained leading to difficulties in correlating structure-property relationships and probing phase behaviour [10]. More recently we have shown that through careful control of the synthetic conditions it is possible to prepare high quality single phase bulk materials which subsequently allowed us to determine the magnetic structure of $\text{Ca}_2\text{Mn}_3\text{O}_8$ for the first time [11]. Given the wide potential applications of these types of materials it is important to fully understand the variable temperature behaviour of $\text{Ca}_2\text{Mn}_3\text{O}_8$ if we are to utilise or optimise (using novel doping strategies) their potential. Recent advances in both the synthesis and *in-situ* diffraction capabilities make it prudent to revisit the thermal stability of $\text{Ca}_2\text{Mn}_3\text{O}_8$ to explore the possibility of intermediate phases and understand the lattice dependence on heating to temperatures above 300 K.

In this paper we report a comprehensive study of the thermal stability of $\text{Ca}_2\text{Mn}_3\text{O}_8$. In-depth *in-situ* powder neutron and X-ray diffraction studies demonstrate that the structure is robust across the whole temperature range studied (200 K to 1123 K). We see no evidence of any atmospheric dependence (either in air, O_2 or N_2) and thermal expansion is isotropic

across the temperature range studied. Electrical measurements show a single response in the impedance spectroscopy consistent with grain behaviour with no evidence for ion conduction. The conduction follows Arrhenius behaviour in the range 350-700 K with activation energy, $E_a = 0.50(1)$ eV consistent with semiconducting behaviour.

2.0 Materials and Methods

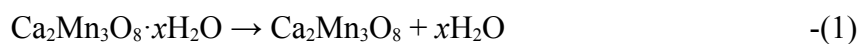
$\text{Ca}_2\text{Mn}_3\text{O}_8$ materials were prepared using the molten-salt method previously reported by us [11]. Briefly, stoichiometric ratios of CaCO_3 and MnCO_3 (both Sigma Aldrich, >99 %) were thoroughly ground together with 350 % w/w of a KCl/NaCl eutectic mixture and heated with intermittent grinding at 973 K for 72 hours (heating rate 10 K/min). Phase purity was determined using a Bruker D8 Advance diffractometer ($10^\circ \leq 2\theta \leq 70^\circ$) equipped with Cu K_α radiation ($\lambda = 1.5406 \text{ \AA}$) operating at 40 kV and 40 mA. Variable temperature X-ray diffraction data were collected between 300 K and 1123 K in air using the Rigaku SmartLab rotating anode $\theta/2\theta$ instrument ($10^\circ \geq 2\theta \geq 70^\circ$) with $\lambda = 1.5406 \text{ \AA}$ and operating at 45 kV and 200 mA. Variable temperature data were collected using an Anton Paar HTK1200N furnace between 300 K and 1323 K (heating rate of 20 K/min between scans) in air. Powder neutron diffraction data were collected on the High Resolution Powder Diffractometer (HRPD) at the ISIS Neutron and Muon Source. Data were collected using three separate sample environments. Initially data were collected over a temperature range of 200 K to 520 K (data collection times of ~4 hours at 200 K and ~2 hours at all other temperatures) within a closed cycle refrigerator (CCR) equipped with a hot stage and with the sample loaded into an aluminium framed slab can masked with Gd. Data were additionally collected between 373 K and 773 K in atmospheres of flowing O_2 and N_2 using a similar method to that previously used by us to study the high temperature phases of BiFeO_3 [24]. $\text{Ca}_2\text{Mn}_3\text{O}_8$ powder compacts were supported within a quartz tube on a quartz frit. The tube was mounted into the furnace with thermocouples resting on the surface of the pellet compacts and the gas flowed over the closed system. Long data collection times (~6 hours) were employed at temperatures of 373 K and 773 K with shorter (15 minute) data collections at intermediate temperatures. Thermal expansion of the lattice parameters were modelled using the function; $\ln a_T/a_0 \approx C_i \theta_i / (\exp(\theta_i/T) - 1)$ where a_0 is the lattice parameter at 0 K, C_i is a constant and θ_i is the Einstein temperature. Simultaneous thermal gravimetry (TG) and differential scanning calorimetry (DSC) measurements were performed in atmospheres of air and nitrogen using the Netzsch STA 409 simultaneous TG-DSC instrument. Data were collected with the

$\text{Ca}_2\text{Mn}_3\text{O}_8$ material loaded into alumina crucibles over a temperature range of room temperature to 1273 K (heating rate 10 K/min). Prior to thermal analysis measurements the materials were dried at 373 K overnight. Raman Spectroscopy data were collected on the Horiba Yobin Labram HR over a temperature range of 298 K to 673 K using the Linkam Examina THMS temperature stage. Data were collected using a 633 nm laser with a 1 second acquisition time integrated over 5 repeat scans using a $\times 50$ objective and 600 lines/nm grating (giving a spectral resolution of $\pm 0.5 \text{ cm}^{-1}$). Dense pellets of $\text{Ca}_2\text{Mn}_3\text{O}_8$ were prepared using the spark plasma sintering (SPS) method. The $\text{Ca}_2\text{Mn}_3\text{O}_8$ pellets were prepared using a 5 mm graphite die at a temperature of 873 K under an applied pressure of 1 GPa. A pellet with a diameter of 5.55 mm, and thickness of 1.5 mm and density $>85 \%$ was obtained. Prior to further analysis the structure of the pellet material was confirmed using powder x-ray diffraction. Electrical measurements were performed using sputtered Au electrodes capped with Ag paint (RS Components) annealed at 393 K for 15 minutes. Dielectric measurements were performed between 50 and 800 K with Agilent 4294A and Wayne Kerr 6500B impedance analyzers over the frequency range of 0.025–2000 kHz. Samples were subjected to heating/cooling rates of 2 K/min in a closed cycle cryocooler or tube furnace. Isothermal impedance spectroscopy measurements were carried out between 300 K to 700 K using a tube furnace and HP 4192A Impedance analyser. All data were corrected for sample geometry.

3.0 Results and Discussion

Room temperature powder X-ray diffraction data confirmed the preparation of high quality $\text{Ca}_2\text{Mn}_3\text{O}_8$, consistent with our previous study, as shown in Figure S1 in the electronic supplementary information (ESI[†]) [11]. In order to investigate the thermal stability of our $\text{Ca}_2\text{Mn}_3\text{O}_8$ we performed simultaneous thermal gravimetry (TG) and differential scanning calorimetry (DSC) measurements in atmospheres of both air and nitrogen. In both cases two distinct weight losses are observed as shown in figure 2. The first weight loss is continuous from room temperature up to a temperature of approximately 573 K in air and 463 K in nitrogen resulting in overall weight losses of 4.0 % and 2.2 % in air and nitrogen respectively. This initial weight loss is attributed to loss of small amounts of water associated with these samples consistent with previous studies on related layered delafossite materials [25]. These materials were prepared by molten salt methods with the post reaction materials filtered and washed with deionised water. Although all materials were dried prior to analysis, it is possible that some water remains and that these materials are not completely dry. The

full formulae are calculated to be $\text{Ca}_2\text{Mn}_3\text{O}_8 \cdot 0.87\text{H}_2\text{O}$ in air and $\text{Ca}_2\text{Mn}_3\text{O}_8 \cdot 0.47\text{H}_2\text{O}$ in nitrogen respectively. The differences in water content in these materials under different atmospheres is reflective that these measurements were performed at different times using different batches of $\text{Ca}_2\text{Mn}_3\text{O}_8$. The second weight loss occurs at temperatures of 1228 K and 1178 K (weight losses of 4.1 % and 5.1 %) in atmospheres of air and nitrogen respectively consistent with that expected for loss of oxygen from these materials (4.3 %) and is accompanied by a strong endothermic peak in the DSC. These features correspond to the decomposition of $\text{Ca}_2\text{Mn}_3\text{O}_8$. These results suggest that $\text{Ca}_2\text{Mn}_3\text{O}_8$ is slightly more stable in air than in reducing atmospheres such as nitrogen. Considering our materials, x-ray diffraction data collected for the final residue (Figure S2 in the ESI) identified the decomposition products as CaMnO_3 and CaMn_2O_4 consistent with the work of Horowitz *et al* [15] and giving the decomposition pathways shown in equations 1 and 2 [15].



Recently, Mazario-Fernandez *et al.* demonstrated the reversible transformation of $\text{Ca}_2\text{Mn}_3\text{O}_8$ to a cubic rocksalt-like, $\text{Ca}_2\text{Mn}_3\text{O}_5$ material under a highly reducing H_2 atmosphere at ~ 770 K with re-oxidation occurring at ~ 1070 K (under O_2) [26]. Whilst it would be expected that N_2 does not provide a strong enough reducing environment to promote the formation of $\text{Ca}_2\text{Mn}_3\text{O}_5$ it may begin to explain the difference in thermal stability observed between reducing and oxidising environments as described above. Considering related delafossite materials the thermal stability behaviour is broad and largely dependent on the types of cations which occupy in the *A* and *B*-sites in ABO_2 . For example AgMnO_2 decomposes into Ag and Mn_2O_3 at a temperature of approximately 900 K [25]. Similar decomposition routes (to a parent Mn_2O_3 and related phases) are also observed in the layered Na_xMnO_2 family of materials and for the ‘*bow-tie*’ lattice Mn_5O_8 [27,28]. By far the most widely studied delafossite family, in terms of their thermal stability, are the CuMO_2 materials (where *M* is Cr, Co, Al, Ga, Fe or Mn) [29-32]. In contrast with the data presented here cuprates behave differently in atmospheres of air and nitrogen [29]. Typically, CuMO_2 materials are stable in atmospheres of nitrogen up to 1373 K (the temperature limit studied) [29]. However, under air a sharp increase in weight is observed for CuGaO_2 , CuCoO_2 , CuFeO_2 and CuMnO_2 (beginning at temperatures between 700 K and 900 K depending on the material) as a result of the oxidative decomposition to CuM_2O_4 and CuO [29-32].

In-situ variable temperature diffraction studies have been performed in order to further probe the thermal stability of $\text{Ca}_2\text{Mn}_3\text{O}_8$. X-ray diffraction data were collected in air between room temperature and 1223 K. Figure 3 shows a comparative plot of selected temperatures. It is clear from these data that the $\text{Ca}_2\text{Mn}_3\text{O}_8$ structure is reasonably robust over the whole temperature range studied with no evidence for intermediate phases consistent with the phase diagram suggested by Horowitz *et al* [15]. To investigate further the temperature dependent structural behaviour of $\text{Ca}_2\text{Mn}_3\text{O}_8$, Rietveld refinements were performed at all temperatures using the GSAS suite of programs [33,34]. All refinements showed excellent fits to the $C2/m$ model proposed by Ansell *et al* [12]. Full refinement details, refined parameters and all refinement profiles are given in the ESI.[†] Close inspection of the lattice parameters and cell volume (Figure 4) show a continuous expansion of the lattice parameters with increasing temperature. Inspection of selected bond lengths and bond angles show that whilst these fluctuate, there is no significant change in these values within error with increasing temperature (as shown in the ESI) confirming there is no significant change in the average structure of $\text{Ca}_2\text{Mn}_3\text{O}_8$ with increasing temperature.[†] We also collected *in-situ* variable temperature powder neutron data on HRPD between 200 K and 520 K, a temperature range which covers the first weight loss regime observed in our thermal analysis data. As with our X-ray diffraction data all patterns can be fitted using the same $C2/m$ model [12] with good agreement observed between the data and the calculated fit. Full refinement details, parameters and profiles are given in the ESI.[†] The lattice parameters and cell volume show a small increase with increasing temperature as expected (see figure S11 in the ESI).[†] Likewise, there is very little variation in either the Mn1-O, Mn2-O3 and Ca-O bond lengths and Mn-O-Mn bond angles as a function of temperature (see figures S12, S13 and S14 in the ESI) consistent with our X-ray diffraction studies. However, a small increase in the Mn2-O1 and Mn2-O2 bond lengths lying in the lattice *b* and *c* directions respectively is observed consistent with the increase in lattice parameters.[†] Modelling the thermal expansion of the lattice parameters (as described in the materials and methods section) demonstrates a volume expansion of approximately 0.7 % as shown in the ESI.[†]

Variable temperature Raman spectra (Figure 5) show no obvious changes with increasing temperature (over the temperature range investigated) consistent with the diffraction data discussed above. We note increasing peak broadening with increasing temperature consistent with increased thermal vibrations. Furthermore, these data are consistent with the spectra reported by Ramirez *et al.* for $\text{Ca}_2\text{Mn}_3\text{O}_8$ films [19]. Using the Bilbao Crystallographic Server we have investigated the expected Raman modes based on the $C2/m$ crystallographic model

[35]. This gives an expected representation of $M = 10A_g + 8A_u + 8B_g + 13B_u$. This can further be broken down into the acoustic modes, $\Gamma_{\text{acoustic}} = A_u + 2B_u$ and optical modes, $\Gamma_{\text{optic}} = 10A_g + 7A_u + 8B_g + 11B_u$, respectively. A total of 15 modes can be observed in our spectra.

In order to further investigate the structural behaviour of $\text{Ca}_2\text{Mn}_3\text{O}_8$ we collected *in-situ* powder neutron diffraction data in atmospheres of both oxygen and nitrogen on HRPD between 373 K and 773 K. Full refinement details, refined parameters and refinement profiles are given in the ESI.[†] As with all the data diffraction data discussed here, an excellent fit to the $C2/m$ model is observed across the whole temperature range independent of atmosphere consistent with that expected from previous studies [12]. A small unindexed peak at a d -spacing of approximately 2.15 Å is observed in all data which arises as a result of vanadium in the sample environment. Likewise, the unusual shape of the background is as a result of the quartz set-up necessary to be able to collect data in gas environments. A smooth increase in the lattice parameters and cell volume with increasing temperature were observed consistent with the X-ray and neutron diffraction data discussed above. Due to the set-up conditions for these experiments we were only able to collect data reliably above a temperature of 373 K. Additionally there is no real change in either bond lengths or bond angles within error. Interestingly, no differences between the data collected under O_2 and N_2 were observed as shown in the ESI.[†] Furthermore, in the high temperature data collected under N_2 we see no evidence for the formation of $\text{Ca}_2\text{Mn}_3\text{O}_5$ consistent with our thermal analysis results [26]. This leads us to conclude that the $\text{Ca}_2\text{Mn}_3\text{O}_8$ structure is indeed robust up to at least 1173 K; unfortunately it has not been possible to probe these materials at the elevated temperatures needed to probe decomposition in our diffraction studies. Modelling of the thermal expansion behaviour (as described in the materials and methods section) results in reasonably large estimated standard deviations (esd) as a result of the small temperature range studied and limited data at low temperatures.[†] However, these data confirm the largely isotropic nature of the expansion consistent with our diffraction studies in air and show no significant differences arising as a result of different atmospheres.

Dielectric permittivity data as a function of temperature on heating and cooling were collected using a sweep mode in order to investigate the temperature dependent electrical behaviour. On heating we note an anomaly in the permittivity between 373 K and 473 K which is not evident on cooling (as shown in figure 6). This is likely due to removal of electrode polarisation effects due to space charge, or loss of water from the material consistent with our thermal analysis data described above. Alternatively, we cannot rule out that these differences may arise as a result of the reducing environments used to prepare the

pellets such that on heating the material is re-oxidised. As expected, we find no evidence for any displacement driven phenomena, such as ferroelectricity, in our data. Impedance spectroscopy data were collected both on heating and cooling between room temperature and 675 K. Data at selected temperatures are plotted as both complex impedance and modulus plane plots in Figure 7. These data indicate a single semi-circular response in both complex impedance (Z^*) and modulus (M^*) plots. The time constant and associated capacitance (*ca.* 3 pF) is the same for the semi-circular arcs in both Z^* and M^* indicating they are attributable to the same electroactive region. From the magnitude of the associated capacitance this is attributed to the bulk response consistent with the preparation of dense ceramics. There is no evidence of a low frequency electrode spike associated with ionic conduction in the Z^* plot, and it is expected that the conductivity is purely electronic. We note that whilst the semi-circle decreases with increasing temperature in the complex impedance indicating a reduction in bulk resistance (R_b), there is little temperature dependence observed in the complex modulus data, indicating a relatively invariant bulk capacitance over the temperature range studied. The bulk conductivity ($\sigma = R_b^{-1}$) is expected to follow Arrhenius behaviour as given by $\sigma = \sigma_0 \exp(-E_a/k_B T)$ where σ is the conductivity, σ_0 is the pre-exponential factor, k_B is the Boltzmann constant, T is the temperature and E_a is the activation energy. Conductivity values were extracted from the complex impedance data and plotted as a function of temperature on both heating and cooling. All data yielded linear relationships of $\log_{10}\sigma$ as a function of inverse temperature as shown in Figure 8; the heating and cooling data are in good agreement with little evidence of hysteresis due to *e.g.* sample degradation. The activation energy was determined to be approximately 0.50(1) eV which is consistent with those reported both experimentally and computationally for other layered transition metal oxides [25,36-38].

4.0 Conclusions

In summary we have performed an extensive variable temperature study of $\text{Ca}_2\text{Mn}_3\text{O}_8$ using thermal analysis, *in-situ* variable temperature X-ray and neutron diffraction, Raman spectroscopy and impedance spectroscopy. Thermal analysis indicates two weight losses at approximately 400 K and 1173 K. The first is indicative of the loss of absorbed water from within the layers or on the surface of the material. The second weight loss is attributed to the decomposition of $\text{Ca}_2\text{Mn}_3\text{O}_8$ into the perovskite, CaMnO_3 and marokite, CaMn_2O_4 phases. Diffraction data demonstrates that the structure is robust across the whole temperature range studied with no change in symmetry. Thermal expansion is largely isotropic within error and

almost little change in the bond lengths and bond angles is observed within the limits of these experiments. The stability of this structure may in some part explain the difficulties in removing Ca^{2+} ions and the kinetic limitations to the redox processes reported for battery measurements [16]. Impedance spectroscopy indicates that the material is an electronic conductor with an activation energy of *ca.* 0.5 eV in the temperature range 400 – 700 K. These studies provide further insight into the thermal stability of $\text{Ca}_2\text{Mn}_3\text{O}_8$ and may be useful for understanding catalytic and battery performance as well as providing a platform for doping strategies and material property optimisation.

5.0 Acknowledgements

The authors acknowledge the ISIS Neutron and Muon User Source for access to beamtime on HRPD (RB1520166 and RB1720182) [39,40]. We are also thankful for access to the instrumentation in the ISIS Materials Characterisation laboratory. We are grateful to Professor Mike Reece at Queen Mary University London for access to the spark plasma sintering (SPS) instrumentation and for assistance preparing pellets. LJV and JAM are grateful for the award of EPSRC DTA studentships.

6.0 Conflicts of Interest

We report no conflicts of interest.

Reference List

- [1] A.P. Amrute, Z. Lodziana, C. Mondelli, F. Krumeich, Perez-Ramirez J., Chem Mater, Chem. Mater. 25 (2013) 4423.
- [2] A.M. Abakumov, A.A. Tsirlin, I. Bakaimi, G. Van Tendeloo, A. Lappas, Chem Mater, Chem. Mater. 26 (2014) 3306.
- [3] A.M.L. Lopez, G.N.P. Oliveira, T.M. Mendonca, J. Agostinho Moreira, A. Almeida, J.P. Araujo, V.S. Amaral, J.G. Correia, Phys. Rev. B. 84 (2011) 014434.
- [4] Q.-L. Liu, Z.-Y. Zhao, Zhao R.-D., J.-. Yi, J. Alloys Compd. 819 (2020) 153032.
- [5] M. Tato, R. Shirnoniski, M. Haglwara, F. Fujihara, ACS Appl. Energy Mater. 3 (2020) 1979.

- [6] S.Y. Wang, G. Wang, X.P. Che, S.F. Wang, C.X. Li, Y.Q. Zhang, Q. Dong, J.S. Qiu, *Environ. Sci. : Nano.* 6 (2019) 2379.
- [7] Q.-. Zhao, Z.-. Zhao, Q.-. Lui, G.-. Yao, X.-. Dong, *J. Phys. D. ; Appl. Phys.* 53 (2020) 135102.
- [8] Y. Chen, Z. Yang, X.G. Jia, Y.H. Wu, N.-. Yuan, J.-. Ding, W.-. Zhang, S.Z. Liu, *Nano Energy.* 61 (2019) 148.
- [9] C. Vecchini, M. Poienar, F. Damay, O. Adamopoulos, A. Daoud-Aladine, A. Lappas, J.M. Perez-Mato, L.C. Chapon, C. Martin, *PRB, Phys. Rev. B.* 82 (2010) 094404.
- [10] L.J. Vera Stimpson, S. Ramos, G.B.G. Stenning, M. Jura, S. Parry, G. Cibin, D.C. Arnold, Investigation of the role of morphology on the magnetic properties of Ca₂Mn₃O₈ materials, *Dalton Trans.* 46 (2017) 14130.
- [11] L.J. Vera Stimpson, E.E. Rodriguez, C.M. Brown, G.B.G. Stenning, M. Jura, D.C. Arnold, Magnetic ordering in a bow-tie lattice full, *J. Mater. Chem. C.* 6 (2018) 4541.
- [12] G.B. Ansell, M.A. Modrick, J.M. Longo, K.R. Poeppelmeier, H.S. Horowitz, *Acta Cryst B, Acta. Crystallogr. B.* 28 (1982) 1795.
- [13] T.R. White, W.S. Glaunsinger, H.S. Horowitz, J.M. Longo, *J. Solid State Chem, J. Solid State Chem.* 29 (1979) 205.
- [14] H.S. Horowitz, J.M. Longo, *Inorg Chem, Inorg. Chem.* 22 (1983) 73.
- [15] H.S. Horowitz, J.M. Longo, *Phase diagram, Mat. Res. Bull.* 13 (1978) 1359.
- [16] Y.J. Park, M.A. Doeff, *Solid State Ionics, Solid State Ionics.* 177 (2006) 893.
- [17] M.M. Najafpour, N. Pashaei S., *Dalton Trans. Dalton Trans.* 41 (2012) 4799.
- [18] M.M. Najafpour, D.J. Sedigh, *Dalton Trans, Dalton Trans.* 42 (2013) 12173.
- [19] A. Ramirez, P. Bogdanoff, D. Friedrich, S. Fiechter, *Nano Energy, Nano Energy.* 1 (2012) 282.

- [20] E. Braktash, I. Zaharieva, M. Schroder, C. Goebel, H. Dau, A. Thomas, Dalton Trans. Dalton Trans. 42 (2013) 16920.
- [21] X. Han, T. Zhang, J. Du, F. Cheng, J. Chen, Chem Sci. Chem. Sci. 4 (2013) 368.
- [22] J. Yang, H. Yu, Y. Wang, F. Qi, H. Liu, L.-. Lou, K. Yu, W. Zhou, S. Liu, Effect of Oxygen coordination environment of Ca-Mn oxides on the catalytic performance of Pd supported catalysts for aerobic oxidation of 5-hydroxymethyl-2-furfural. Catal. Sci. Technol. 9 (2019) 6659.
- [23] A. Gagrani, M. Alsultan, G.F. Swiegers, T. Tsuzuki, Comparative evaluation of the structural and other features governing phot-electrochemical oxygen evolution by Ca/Mn oxides, Catal. 10 (2020) 2152.
- [24] D.C. Arnold, K.S. Knight, G. Catalan, S.A.T. Redfern, J.F. Scott, P. Lightfoot, F.D. Morrison, Adv. Funct. Mater. Adv. Funct. Mater. 20 (2010) 2116.
- [25] O. Mahroua, B. Alili, A. Ammari, B. Ballal, D. Bradai, M. Trari, AgMnO₂, Ceram Int. 45 (2019) 10511.
- [26] A. Mazario-Fernandez, A. Torres-Pardo, A. Verela, M. Parras, J.L. Martinez, M.T. Fernandez-Diaz, M. Hernando, J.M. Gonzalez-Calbet, Ca₂Mn₃O₅, Inorg. Chem. 56 (2017) 11753.
- [27] I. Bakaimi, R. Brescia, C.M. Brown, A.A. Tsirlin, M.A. Green, A. Lappas, Na_{0.7}MnO₂ hydrate, Phys. Rev. B. 93 (2016) 184422.
- [28] P. Zhang, J. Liu, K. Page, A. Navrotsky, Mn₅O₈ thermal, J. Am. Ceram. Soc. 102 (2019) 1394.
- [29] A.P. Amrute, Z. Lodziana, C. Mondelli, F. Krumeich, Perez-Ramirez J., Solid-state chemistry of cuprous delafossites: synthesis and stability aspects, Chem. Mater. 25 (2013) 4423.
- [30] Z. Du, D. Xiong, S.K. Verma, B. Liu, X. Zhao, L. Liu, H. Li, CuCoO₂, Inorg. Chem. Front. 5 (2018) 183.

- [31] J. Schorne-Pinto, L. Cassayre, L. Presmanes, A. Barnabe, CuFeO₂, *Inorg. Chem.* 58 (2019) 6431.
- [32] D. Xiong, Q. Zhang, Z. Du, S.K. Verma, H. Li, X. Zhao, CuMnO₂, *New J. Chem.* 40 (2016) 6498.
- [33] B.H. Toby, *J. appl. crystal, J. Appl. Crystallogr.* 34 (2001) 210.
- [34] A.C. Larson, R.B. von Dreele, Los Alamos National Laboratory Report (LAUR), Los Alamos National Report LAUR. 96 (1994) 86.
- [35] E. Kroumova, M.I. Aroyo, J.M. Prez-Mato, A. Kirov, C. Capillas, S. Ivantchev, H. Wondratschek, *Bilbao Crystallographic Server, Phase Transitions.* 76 (2003) 155.
- [36] Q.-. Liu, Z.-. Zhao, R.-. Zhao, J.-. Yi, Band gap CuFeO₂, *J. Alloys Compd.* 819 (2020) 153032.
- [37] G. Pananpitiya, G. Avendano-Franco, J.P. Lewis, AgMnO₂ band gap, *Comput. Mater. Sci.* 170 (2019) 109173.
- [38] T. Zhao, A.L. Liu, Z.-. Zhao, Band gap, *J. Phys. Chem. C.* 123 (2019) 14292.
- [22] <https://doi.org/10.5286/ISIS.E.RB1520166>.
- [23] <https://doi.org/10.5286/ISIS.E.RB1720182>.

List of Figures

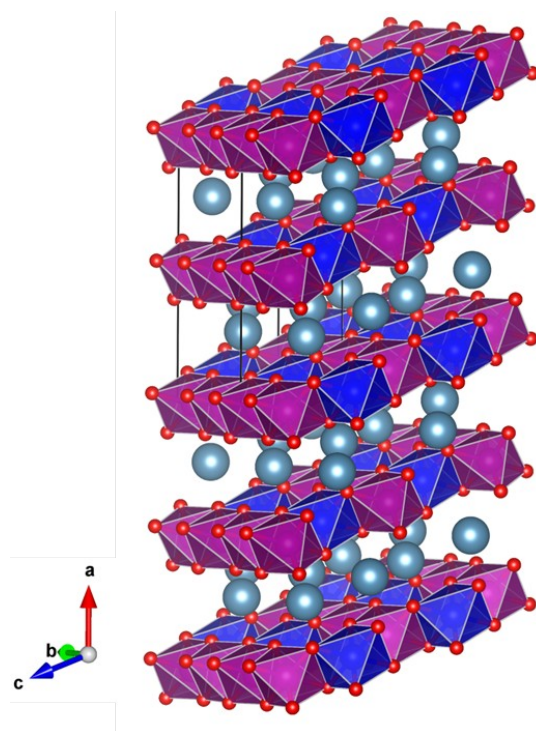


Figure 1: Schematic representation of the crystal structure of $\text{Ca}_2\text{Mn}_3\text{O}_8$. The blue spheres and polyhedra represent the manganese ion and MnO_6 octahedra on the Mn1 crystallographic site and the pink spheres and polyhedra represent the manganese ion and MnO_6 octahedra on the Mn2 crystallographic site. Each of the layers exhibits a crystallographic void, the position of which alternates between the layers. The teal and red spheres are the Ca^{2+} and oxygen ions respectively.

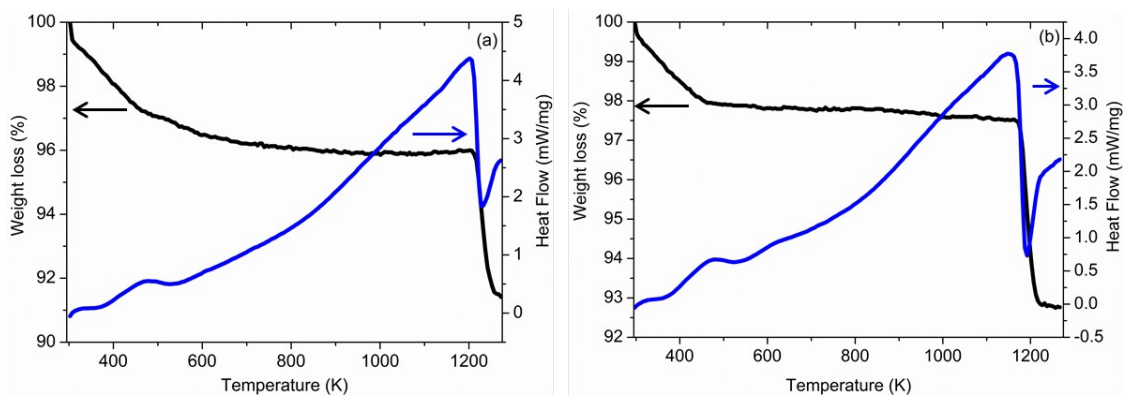


Figure 2: Thermal gravimetry (TG) and differential scanning calorimetry (DSC) data collected between room temperature and 1273 K for $\text{Ca}_2\text{Mn}_3\text{O}_8$ in atmospheres of (a) air and (b) nitrogen.

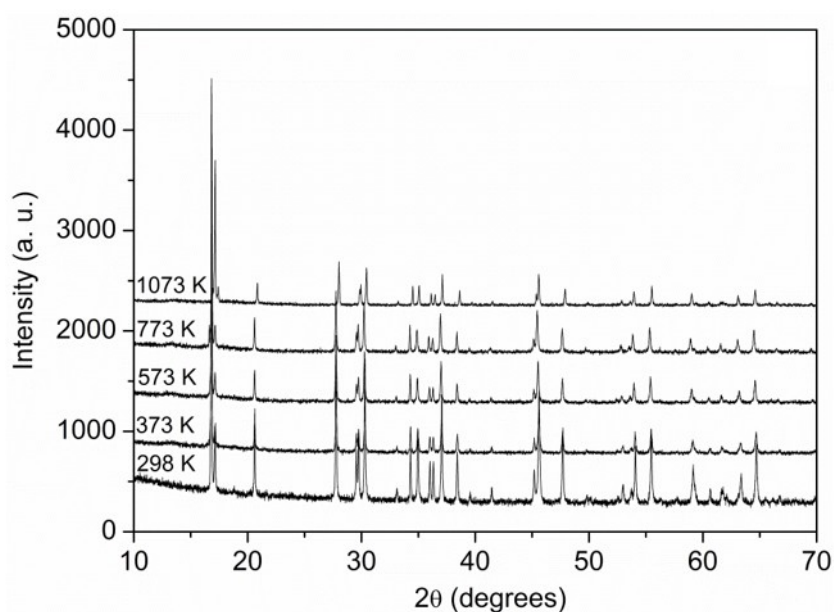


Figure 3: Comparative plot of X-ray diffraction data collected for $\text{Ca}_2\text{Mn}_3\text{O}_8$ as a function of temperature showing no appreciable change in crystal structure over the temperature range studied.

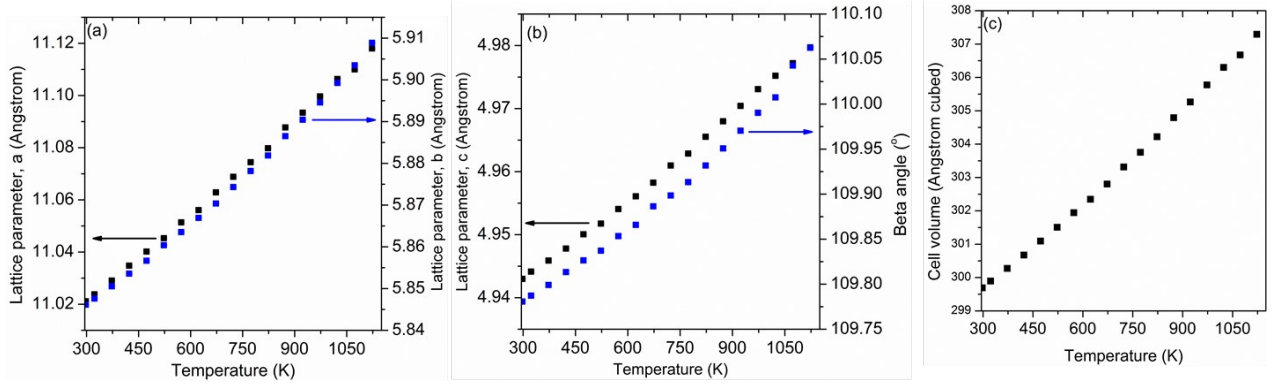


Figure 4: Lattice parameters (a) a and b , (b) c and beta angle and (c) cell volume as a function of temperature extracted from the Rietveld refinement using X-ray diffraction data collected for $\text{Ca}_2\text{Mn}_3\text{O}_8$. Note error bars are smaller than the symbol size.

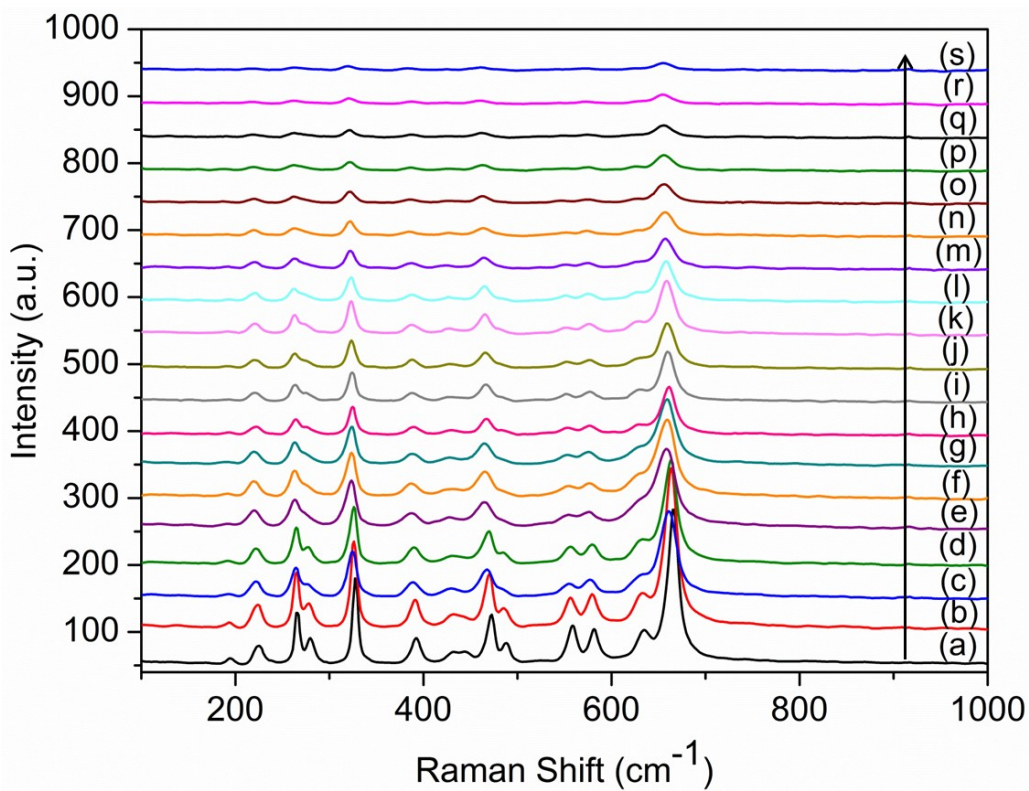


Figure 5: Comparative plot of Raman spectra collected between 300 K and 673 K showing no obvious change in symmetry with increasing temperature (the arrow shows increasing temperature) with data collected at (a) 300 K, (b) 323 K, (c) 353 K, (d) 373 K, (e) 393 K, (f) 413 K, (g) 433 K, (h) 453 K, (i) 473 K, (j) 493 K, (k) 513 K, (l) 533 K, (m) 553 K, (n) 573 K, (o) 593 K, (p) 613 K, (q) 633 K, (r) 653 K and (s) 673 K.

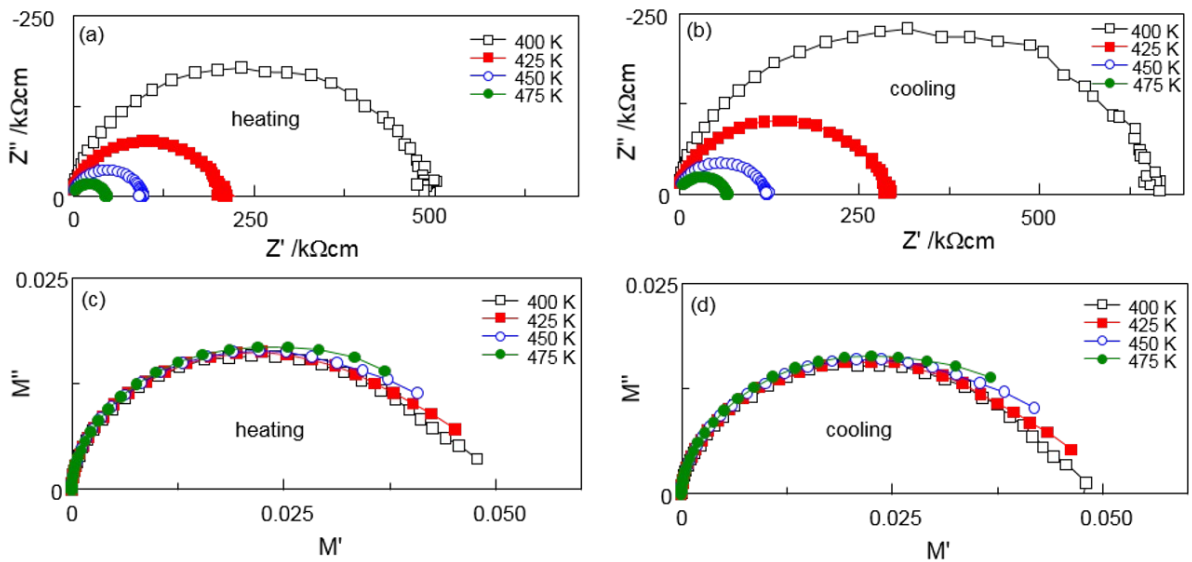


Figure 6: Variable temperature impedance spectroscopy data for $\text{Ca}_2\text{Mn}_3\text{O}_8$ on both heating and cooling plotted in the complex impedance, Z^* , (a and b) and complex modulus, M^* , (c and d) planes.

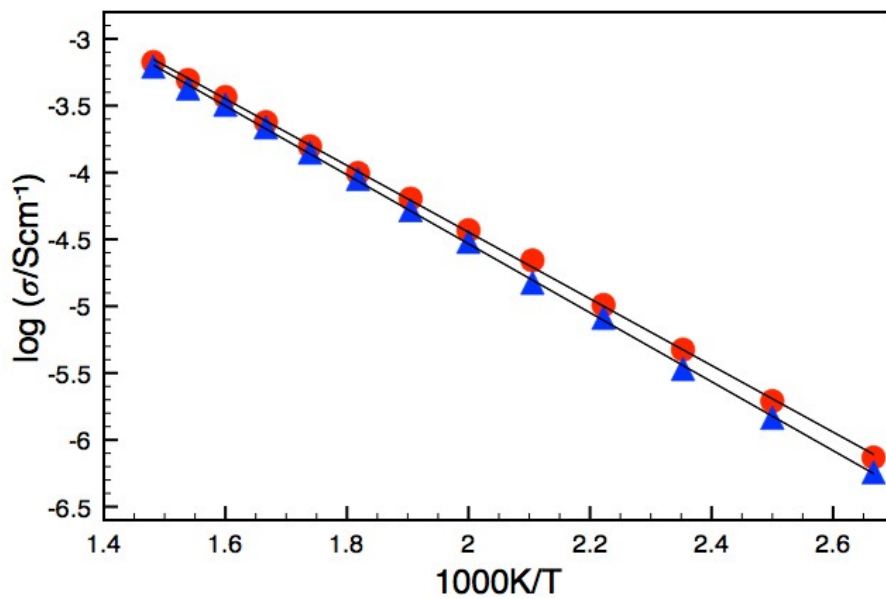


Figure 7: Arrhenius plots of bulk conductivity vs. reciprocal temperature on heating (red circles) and cooling (blue triangles).